Origin of the Griffiths phase and correlation with the magnetic phase transition in the nanocrystalline manganite $La_{0.4}(Ca_{0.5}Sr_{0.5})_{0.6}MnO_3$

Suvayan Saha [1,2,*] Apurba Dutta,[3] Shuvankar Gupta,[3] Sudipta Bandyopadhyay [1,2] and I. Das[3]

[1]*Centre for Research in Nanoscience and Nanotechnology, University of Calcutta, JD-2, Salt Lake City, Kolkata-700098, West Bengal, India*

[2]*Department of Physics, University of Calcutta, 92 A.P.C. Road, Kolkata 700009, India*

[3]*CMP Division, Saha Institute of Nuclear Physics, A CI of Homi Bhabha National Institute, 1/AF, Bidhannagar, Kolkata 700 064, India*

(Received 18 July 2021; revised 23 April 2022; accepted 20 May 2022; published 7 June 2022)

In this paper, a detailed comprehensive magnetic study on the origin of the Griffiths phase (GP) in the nanocrystalline $La_{0.4}(Ca_{0.5}Sr_{0.5})_{0.6}MnO_3$ compound has been presented. The system exhibits a ferromagnetic (FM)-like transition around $T_C \sim 274$ K. Interestingly, above T_C, the state is not pure paramagnetic, but a short-range FM interaction or GP is observed and the interaction persists up to the Griffiths transition temperature, $T_G \sim 350$ K. The detailed investigation of isothermal magnetization and the magnetocaloric effect along with its theoretical analysis have been employed besides the conventional magnetic measurements to probe the GP. Disorder in the system is introduced via increasing an A-site cationic size mismatch along with an additional defect originated owing to the particle size reduction. The disorder-induced magnetic phase transition has also been analyzed by critical analysis. A correlation between the unusual critical parameters with the GP has been furnished.

DOI: 10.1103/PhysRevB.105.214407

I. INTRODUCTION

Griffiths phase (GP) is a short-range ordering of ferromagnetic (FM) clusters existing above the long-range magnetic ordered region of a system [1–8]. This well-accepted phenomenon was originally proposed theoretically by Griffiths while describing randomly diluted Ising ferromagnets whose lattice sites are partially occupied with spins and the remaining portions are either filled with nonmagnetic ions or vacant [9]. Experimentally, the GP behavior is observed to appear in diverse systems, e.g., transition-metal oxides (electron-/hole-doped manganites [1,2,5,10–13], layered manganites [14], doped cobaltite [15] etc.), double perovskite compounds [16–18], intermetallic systems [4,7,19], heavy Fermi materials [3], etc., and, in addition, a Griffiths-like phase can also emerge in other physical scenarios, such as in brain criticality [20] and in the Mott transition (electronic GP) systems [21,22]. The singularities would grow in the temperature regime $T_C < T < T_G$, where T_C is magnetic transition temperature and the new temperature scale, T_G, has been coined as the Griffiths temperature. In this regime, the system does not show a true paramagnetic (PM) behavior or a long-range FM ordering. Hence, the underlying physics is considered to be very rich in the temperature range between T_C and T_G [23–26].

Experimentally, it is also found that the existing quench disorder in a system plays a major role in developing the GP [1,2,5,8]. In such systems, there exists few specially distributed finite regions, where owing to the scarce of disorder, FM correlated spins form finite-size clusters and, thereby, instead of maintaining a spontaneous magnetization, the system exhibits a short-range FM interaction and the magnetic singularity is noticed above T_C. One such system is doped manganite. The research in this area has been rejuvenated in doped manganites, while the observed colossal magnetoresistance (CMR) phenomenon has been predicted and explained within the context of Griffiths singularity [1,10]. Though there is an ongoing debate on whether the GP is always a prerequisite for CMR [27], as the presence of magnetic phase inhomogeneity is considered to be crucial to explain CMR related properties and, on the other hand, this magnetic inhomogeneity that appears from the existing disorder induced strong correlation between charge, spin, and lattice degrees of freedom also assists in growing the GP in the system [1,27]. The factors that drive the disorder in such systems are divalent doping concentrations that perturb the Mn^{3+}/Mn^{4+} ratio [2], magnetic site dilution [8], and Jahn-Teller (J-T) distortion, originating from J-T active ions Mn^{3+} [11,28,29], A-site cationic size mismatch along with the variance of size disorder parameter (σ^2) [5,30,31], etc. The enhanced σ^2 destabilizes the Mn–O–Mn bond angle, bond length in a system, and, hence, this bond disorder also transmits and interrupts the magnetic Mn–O–Mn network. Thus, these intrinsic factors play a vital role in creating sufficient disorder as well as inhomogeneity in the system and helps to stabilize a GP [1,2,5].

In doped manganite systems, an additional disorder can be introduced via reducing its particle size, i.e., grains are constructed by preparing nanomaterial [32–36]. The formation of intergranular distance or grain boundary acts as a defect in the nanocrystalline compound [32,37]. This defect can further add up disorder that may destabilize the long-range ordering in the system by affecting the Mn–O–Mn chain and may also act as a trigger of appearing GP. Moreover, disorder in this type of system is known to drive a first-order transition

*Email address: suvayan.phy@gmail.com

toward second-order transition, i.e., discontinuous to continuous transition [27,38,39].

To comprehend the nature of the magnetic phase transitions in any magnetic system, the critical analysis around the transition temperature is recognized to be a powerful mechanism to employ [40,41]. The magnetization of a continuous or second-order phase transition is described by the various critical exponents (β, γ, δ) extracted from the rigorous critical analysis. The different sets of critical exponent values that belong to various universality classes fundamentally characterize the nature of magnetic interactions in a system [40,41]. Additionally, to provide further evidence of existing intrinsic magnetic inhomogeneity [42–44] in the system and also to characterize the stability of the GP [5,10,27], critical exponent values are worth exploring.

As the GP phenomenon is observed above the magnetic transition temperature in a system, it is useful to characterize it using susceptibility critical exponent, γ. However, theoretically, all the exponents are interrelated via different relations [43,44] and, therefore, the GP must have an impact on the magnetic transitions as well as the magnetization in the $T < T_C$ region in a system. Hence, establishing the correlation of the GP with a magnetic phase transition utilizing comprehensive critical analysis is an interesting subject matter to explore.

In this paper, through detailed magnetic and magnetocaloric effect (MCE) studies, we have shown that the nanocrystalline $La_{0.4}(Ca_{0.5}Sr_{0.5})_{0.6}MnO_3$ (LCSMO) compound exhibits GP behavior above FM-like transition at $T_C =$ 274 K. It is worth mentioning here that the bivalent higher cationic size radius Sr is doped at the Ca site of the parent $La_{0.4}Ca_{0.6}MnO_3$ (LCMO) system to prepare the bulk LCSMO compound which is reported to exhibit an antiferromagnetic (AFM) transition at $T_N = 235$ K [45]. The doping creates disorder (mismatch) between the elements at the A site of the LCSMO compound [45]. As we discussed earlier, via reducing the particle size, one can introduce additional disorder in the system, which in turn helps to originate and stabilize a GP, if any; we choose a nanocrystalline LCSMO compound to explore the GP behavior. The presence of the GP or a magnetically ordered rare region has been elucidated primarily by the popular route of plotting an inverse susceptibility curve as a function of temperature. Subsequently, various other magnetic measurements including magnetocaloric effect have been utilized to substantiate it. These magnetization data have also been analyzed with proper theoretical model to further support the GP. Moreover, the critical analysis of the compound has also been carried out to comprehend the nature of the different magnetic transitions. The origin of the GP as well as its correlation with the magnetic phase transition has also been corroborated here.

II. SAMPLE PREPARATION AND CHARACTERIZATION

The nanocrystalline LCSMO compound has been prepared by following the well-known sol-gel method [46]. Preheated rare-earth oxide (La_2O_3), carbonate ($CaCO_3$), nitrate [$Sr(NO_3)_2$] and MnO_2 have been taken with proper stoichiometry. These starting materials were greater than 99.99% pure. Concentrated HNO_3 was used to dissolve La_2O_3 and $CaCO_3$ and nitrate salt was dissolved in millipore water. To dissolve MnO_2, oxalate was first prepared by mixing oxalic acid and then concentrated HNO_3 was added. All solutions were kept for hours to dissolve properly and then, they were mixed together in moderate heating and constant stirring conditions. After that, a suitable amount of citric acid was added and stirred again for 15 min. The clear solution was then put into a heat bath maintained at 80–90 °C until the gel was formed. Then the beaker with gel was put to the heater directly at 200–220 °C. The gel was then turned into a black porous powder after getting self-ignited. The collected black powder was further heat treated for 5 h at 400 °C to remove organic residue. Finally, pellets were prepared and, to get nanomaterial, it was heat treated at 900 °C for 4 h.

Room temperature x-ray diffraction for phase confirmation as well as structural characterization was done utilizing a Rigaku Diffractometer with Cu-K_α ($\lambda = 1.54$ Å) source. The stoichiometric composition of the element (given in the Supplemental Material [47]) was checked using a scanning electron microscope, Carl Zeiss, Germany with energy dispersive x-ray analysis.

Magnetization measurements were performed with a SQUID-VSM between 3–400 K temperature range and up to 70 kOe magnetic field variation.

A bar-shaped LCSMO sample was used for the magnetic measurements and the dimension of the sample was $4 \times 2 \times 1$ $(mm)^3$.

III. EXPERIMENTAL RESULTS AND DISCUSSIONS

A. Magnetization, magnetic phase transition, and critical analysis

Temperature variation of zero-field-cooled (ZFC) and field-cooled (FC) dc magnetization [*M(T)*] from 3 K to 370 K, under magnetic field, $H = 500$ Oe, has been performed and shown in Fig. 1. The bifurcation is noticed between ZFC-FC curves below $T \sim 240$ K. The observed transition is FM-like in nature and the transition temperature, T_C (~ 280 K) is determined from the dM/dT versus T curve shown in the lower part of Fig. 1. The minima in dM/dT versus T plot expanded almost 100 K span of temperature. It indicates that the transition is not a long-range FM type and above T_C, a possible short-range magnetic interaction present in the system. Thus, to understand the magnetic nature of the high temperature region while approaching toward magnetic phase transition, along with the type of long-range ordering of the transition and its universality class, the critical analysis around the FM phase transition temperature of the compound has been carried out. The strength and nature of the magnetic interactions can also be extracted from the analysis [43,48]. Usually, the critical exponents and critical temperature of a system are determined by analyzing the Arrott plot, i.e., M^2 versus H/M around T_C [49]. To find out the order of the transition, the Banerjee criterion has been followed [50]. According to this, the positive (negative) slope of the high field M^2 versus H/M curves implies the second-order (first-order) phase transition. The *M(H)* isotherms for the compound taken around the T_C have been shown in Fig. 2(a) and these curves clearly exhibit a continuous FM-like phase transition. The positive slope

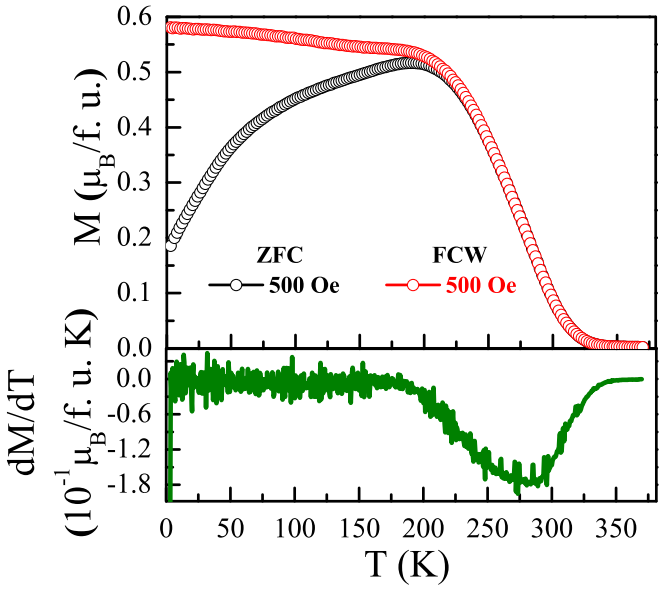

FIG. 1. Temperature dependence of ZFC-FC magnetization in presence of $H = 500$ Oe. Below: dM/dT of FC curve ($H = 500$ Oe) as a function of temperature.

in the Arrott plot [shown in Fig. 2(b)]also substantiates the continuous or second-order magnetic phase transition in the compound. Though the isotherms in M^2 versus H/M plot are almost linear, a slight downward deviation in the curves is noticed that interrupts to find the actual (critical) isotherm, which passes through the origin. Hence, the modified Arrott plot (MAP) method, provided by Arrott-Noaks [51], has been employed to investigate the critical behavior of susceptibility as well as magnetization near T_C. The equation is given by

$$(H/M)^{1/\gamma} = a\left(\frac{T - T_C}{T_C}\right) + bM^{1/\beta} \tag{1}$$

here, a and b are constants. It is well established that, near the critical temperature of a continuous PM to FM transition, the critical nature of susceptibility and magnetization can be classified using the appropriate values of critical exponents, i.e., β, γ, and δ [43,48,52]. The spontaneous magnetization $[M_S(0, T) = M_{H=0}]$, initial susceptibility $[\chi_i(0, T) = \partial M/\partial H_{H=0}]$, and magnetization at T_C $[M(H, T_C)]$ follow the power-law behavior and the relations having the forms [52]

$$M_S(0, T) = M_S(0)(-\varepsilon)^{\beta}, \varepsilon < 0, \tag{2}$$

$$\chi_i(0, T) = \chi_0(\varepsilon)^{-\gamma}, \varepsilon > 0, \tag{3}$$

$$M(H, T_C) = A(H)^{1/\delta}, \varepsilon = 0, \tag{4}$$

where $\varepsilon = (T - T_C/T_C)$ is the reduced temperature, which is a dimensionless quantity. $M_S(0)$, χ_0, and A are the critical amplitudes in the corresponding equations, with H being the internal magnetic field. The universal characteristic of a material is decided by these critical exponents and critical amplitudes near the magnetic phase transition point. To find out the appropriate values of β and γ, first the magnetic isotherms of the $(H/M)^{1/\gamma}$ versus $M^{1/\beta}$ have been plotted with initial values of β and γ taken from the theoretical models. The value of these exponents are then refined until a set of quasistraight lines and an approximate critical isotherm, i.e., where the $T = T_C$ curve passes almost through the origin, are achieved. These isotherms intercept on x and y axes and, respectively, yield $\chi_i(0, T)^{-1/\gamma}$ (for $T > T_C$) and $M_S(0, T)^{1/\beta}$ (for $T < T_C$). These obtained $M_S(0, T)$ and $\chi_i(0, T)$ data have been tested using aforementioned power laws. With taking the initial value of T_C estimated from the previous MAP fitting, these values are fitted using Eqs. (2) and (3) to get improved values of β, γ, and T_C. A new MAP has been again constructed using the estimated critical exponent values that improves the values of γ, β, and T_C further. This refinement has been carried out until consistent values of T_C, β, and γ are achieved [40]. The MAP for the temperature range $T = 264$ K to 286 K is shown in Fig. 3(a). Only higher field region data of these isotherms have been fitted to avoid the unnecessary contribution of the demagnetization factor and the magnetic domains' rearrangement at the low-field region in the calculation. The estimated critical exponent values are $\beta = 0.61$ and $\gamma = 1.09$. The extracted critical isotherm that passes through the origin has been considered to be $T_C \simeq 274$ K. Moreover, the M_S and χ_0^{-1} for different temperatures have been obtained following the aforementioned process. The power-law fitting of the $M_S(T)$ curve yields $\beta = 0.604 \pm 0.003$ with $T_C = 274.00 \pm 0.08$, on the other hand, χ_0^{-1} yields $\gamma = 1.096 \pm 0.006$ with $T_C = 274.34 \pm 0.16$. The fitted plots are shown in Fig. 3(b). The extracted values of critical exponents β, γ, and magnetic transition temperature T_C match well with the values estimated from MAP that supports the reliability of the calculation as well as the trueness of the values. In addition to that, the Kouvel-Fisher (KF) [53] method has been used further to check the correctness of these β, γ, and T_C values. According to this technique,

$$M_S(T)[dM_S(T)/dT]^{-1} = (T_C - T)/\beta, \tag{5}$$

$$\chi_0^{-1}(T)[d\chi_0^{-1}/dT]^{-1} = (T - T_C)/\gamma. \tag{6}$$

Using these relations, $|M_S(T)[dM_S(T)/dT]^{-1}|$ and $\chi_0^{-1}(T)[d\chi_0^{-1}/dT]^{-1}$ have been plotted as a function of temperature that produces straight lines having slopes $1/\beta$ and $1/\gamma$, respectively. The intercept of these lines on the temperature axis yields T_C. Hence, using the KF method, these curves have been fitted linearly, which gives $\beta = 0.61 \pm 0.02$ with $T_C = 274.18 \pm 0.08$ from Eq. (5) and $\gamma = 1.11 \pm 0.04$ with $T_C = 274.36 \pm 0.29$ from Eq. (6). All the data including linear fitted plots have been shown in Fig. 3(c). These values also match well with the previously estimated critical values. The other critical exponent (δ) has been extracted from the isothermal magnetization at $T = T_C$ utilizing Eq. (4). The M-H curve closest to T_C ($T = 274$ K) is shown in Fig. 3(d). The inset of Fig. 3(d) exhibits the linear fitted curve at the high magnetic field region of the log-log M-H plot. δ is determined from the slope $(1/\delta)$ of that fitted straight line and the value is 2.789 ± 0.001. The deviations in the analysis of least-squares fitting of the critical behavior investigation have been considered as error bars. Moreover, these β, γ, and δ also follow the Widom scaling relation [54,55]:

$$\delta = 1 + \gamma/\beta. \tag{7}$$

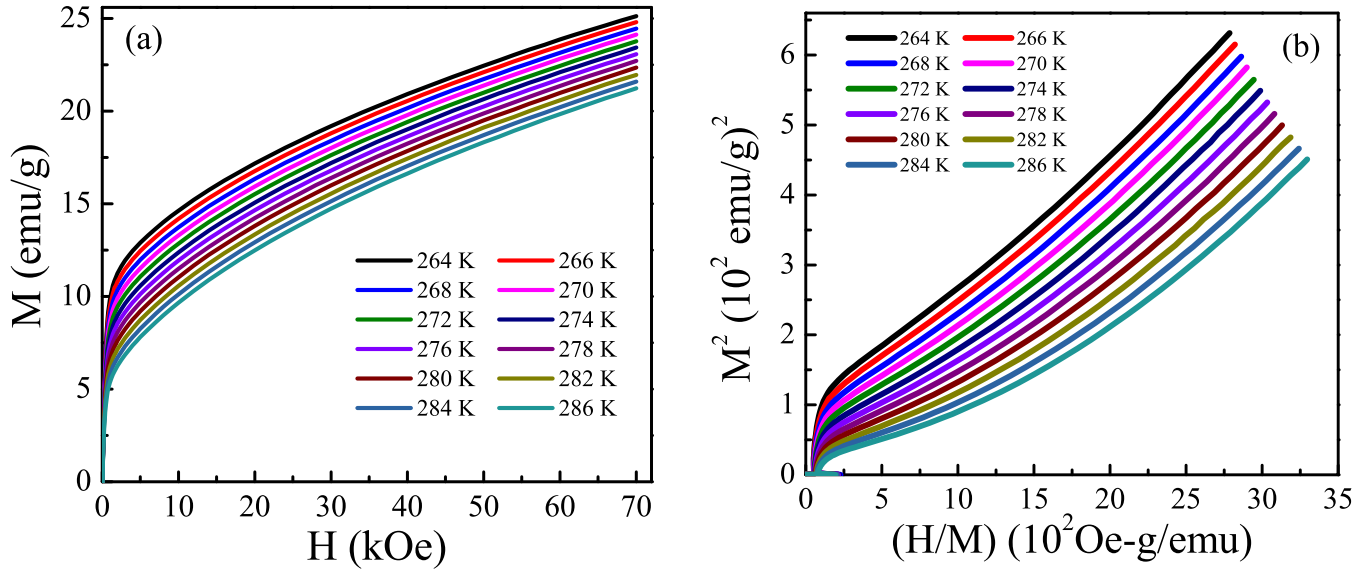

FIG. 2. (a) Isothermal magnetization curves [$M(H)$] at different constant temperatures around T_C. (b) Arrott plots of corresponding isotherms (M^2 versus H/M).

Putting the obtained critical exponents from MAP [Fig. 3(b)] and KF [Fig. 3(c)] methods in the relation, the δ values have been calculated as 2.814 ± 0.009 and 2.819 ± 0.06, respectively. The obtained δ values are almost close to the calculated δ value from the isothermal magnetization fitting in Fig. 3(d). Therefore, the consistency of the Widom scaling with the previously observed critical exponents again supports the reliability of the critical analysis.

The most meticulous technique to check the correctness and reliability of these observed critical exponents as well as T_C is to match the data with the scaling hypothesis [52]. The equation of the hypothesis is as follows:

$$M(H, \varepsilon) = (\varepsilon)^{\beta} f_{\pm}[H/\varepsilon^{(\gamma+\beta)}], \tag{8}$$

where f_+ and f_- are the scaling functions for $T > T_C$ and $T < T_C$, respectively. Hence, Eq. (8) indicates that, for the appropriate choice of β, γ, and δ values, the $M|\varepsilon|^{-\beta}$ versus $H|\varepsilon|^{-\beta+\gamma}$ isotherms around T_C generate two universal curves for the temperatures below and above T_C. For better results, the log-log plot of these isotherms has been shown in Fig. 4, where these isotherms fall onto two individual curves for $T < T_C$ and $T > T_C$. Thus, two branches of these isotherms around T_C clearly prove the universality nature and further substantiate the trueness of the calculation of critical analysis. The critical exponents, which are estimated using different techniques, are listed and compared with different theoretical models in Table I.

Note from the comparison in Table I that, though the critical exponent values for the compound nearly follow the mean-field model compared to the other well-known theoretical models, the values of β, γ are greater than and δ is less than the predicted mean-field model. Moreover, the γ value may be considered to be lying between the mean-field and 3D Ising models, implying that all magnetic moments in the LCSMO compound are neither exclusively influenced by the identical averaged exchange field induced by all neighbors (i.e., the mean-field model) nor the magnetic moments influenced by only 1D nearest-neighbor spin interaction (i.e., 3D Ising model) [56]. It could be owing to the presence of defects, originating from the enhanced A-site disorder as well as formation of nanograins and/or grain boundaries, resulitng in the appearance of short-range FM interaction (GP), amidst the global PM matrix, creating an additional critical exponent correlation length scale in the LCSMO system. Thus, the observed particular γ value (~ 1.09) in the system could be a collective result of more than one correlation length [57]. Physically, β portrays the growth of the ordered moment below T_C, with smaller values reflecting faster growth; δ illustrates the curvature of magnetic isotherm at T_C, with smaller values implying less curvature, including slower saturation, and γ provides the information of the divergence of initial magnetic susceptibility while approaching T_C from $T > T_C$, with smaller values indicating sharper divergence. However, γ is also considered to be a measure of the FM interaction range in a system and Fisher *et al.* [58] theoretically developed the meticulous relation between the susceptibility exponent (γ) and the range of exchange interaction (σ) having the form

$$\gamma = 1 + \frac{4}{d}\left(\frac{n+2}{n+8}\right)\Delta\sigma + \frac{8(n+2)(n-8)}{d^2(n+8)^2} \times \left[1 + \frac{2G\left(\frac{d}{2}\right)(7n+20)}{(n-4)(n+8)}\right]\Delta\sigma^2. \tag{9}$$

Here d and n stand for the dimension of the lattice and the spin in the system, respectively, $\Delta\sigma = (\sigma - \frac{d}{2})$ and $G(\frac{d}{2}) = 3 - \frac{1}{4}(\frac{d}{2})^2$.

Accordingly, the isotropic exchange interaction [$J(r)$] between spins has an impact on the universality class of the magnetic phase transition in a long-range FM system. As per the renormalization (group theory) analysis for these kinds of systems, $J(r) \sim 1/r^{d+\sigma}$, where, r is the distance and d and σ have been mentioned earlier. When, $\sigma > 2$, the $3D$ Heisenberg exponents (given in Table I) are valid and $J(r)$ decreases with r faster than $1/r^5$. On the other hand, the mean-field exponents (given in Table I) hold when $\sigma < 3/2$ and $J(r)$

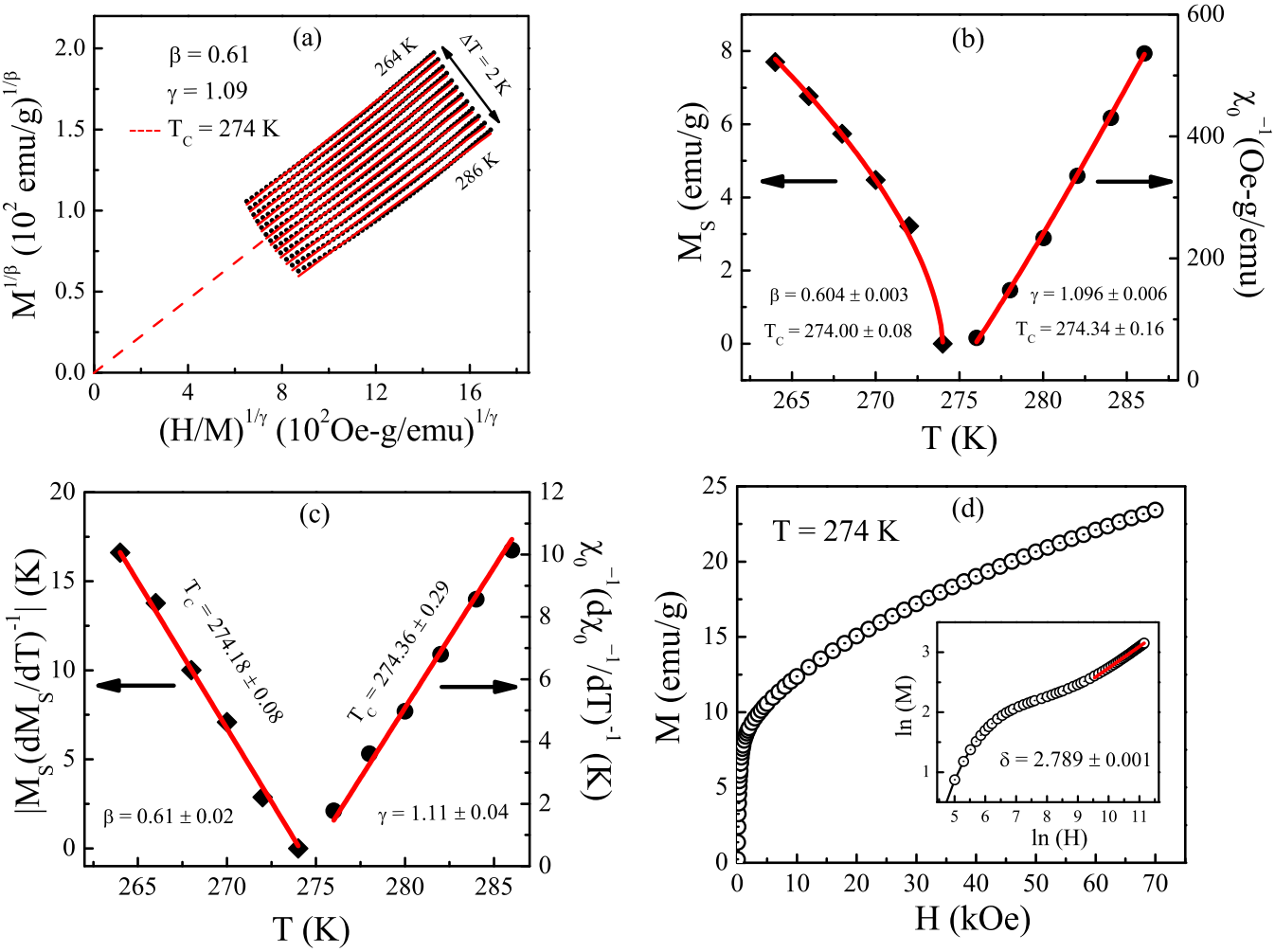

FIG. 3. (a) Modified Arrott plot isotherms [$M^{1/\beta}$ versus $(H/M)^{1/\gamma}$] around T_C. Solid red lines indicate the high field linear fit of these isotherms and dashed red line almost passing through the origin indicates the estimated T_C. (b) Temperature variation of spontaneous magnetization [$M_S(T)$] (left axis) and inverse initial magnetic susceptibility [$\chi_0^{-1}(T)$] (right axis). Solid lines are the fitted curves obtained using the power-law in Eqs. (2) and (3). (C) $M_S(T)$ and $\chi_0^{-1}(T)$ plots, observed with the help of Kouvel-Fisher method. Solid lines are the linear fitting of those data. (d) Critical isotherm $M(H)$ close to the T_C (274 K). Inset: Same plot in log-log scale. Solid line is the linear fit using Eq. (4).

reduces with r slower than $1/r^{4.5}$. Hence, for three-dimensional systems, the aforementioned interaction expression turns out to be $J(r) \sim 1/r^{3+\sigma}$, with $3/2 \leqslant \sigma \leqslant 2$ for intermediate ranges and the exponents for this range belong to a different universality class that depends on σ. Thus, σ as well as the spin interaction around the magnetic phase transition of the system has been estimated by utilizing the aforementioned expression. The parameter σ in Eq. (9) has been adjusted in such a way that it yields the γ value approximately same as observed via experiments (i.e., $\gamma \sim 1.09$) for a specific value of d and n. Thus, taking lattice dimension, $d = 3$, the relevant results for $n = 1, 2, 3, \infty$ are observed [58,59].

TABLE I. Comparison of various determined critical parameters with different well-established theoretical models.

System	Reference	Technique	β	γ	δ	T_C (K)
LCSMO	This paper	Modified Arrott plot	0.604 ± 0.003	1.096 ± 0.006	2.814 ± 0.009	274
		Kouvel-Fisher	0.61 ± 0.02	1.11 ± 0.04	2.819 ± 0.06	
		Critical isotherm			2.789 ± 0.001	
3D Ising	[40,41,56]	Theoretical	0.325	1.241	4.82	
3D Heisenberg	[40,41,56]	Theoretical	0.365	1.386	4.8	
Mean field	[40,41,56]	Theoretical	0.5	1	3	
3D XY	[56]	Theoretical	0.345	1.316	4.81	

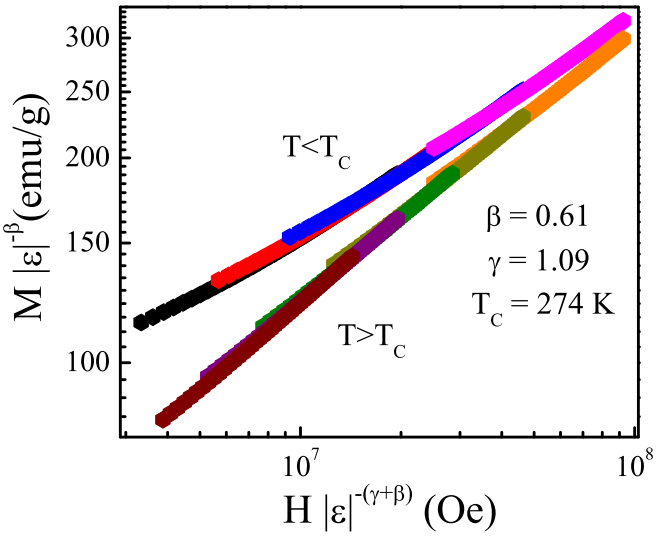

FIG. 4. Log-log scaling plot using estimated β and γ values.

Multiple interaction ranges corresponding to different n values are observed for the system and the values lie in the range $3/2 \leqslant \sigma \leqslant 2$ (shown in the Supplemental Material). Hence, it may be concluded that the observed critical exponents belong to a different universality class. Therefore, to delve further to inquire if these critical phenomena describe any new (or weak) universality class in the system, the investigation has been further extended to the analysis proposed by Suzuki [60] where, instead of taking the exponents of temperature difference, the correlation lengths, $\xi(T)(= \text{const} \mid T_C\text{-}T \mid^{-\nu})$ corresponding to different σ (interaction ranges) have been taken into consideration. ξ is linked with σ via correlation length exponent (ν) having the form $\nu = \frac{\gamma}{\sigma}$ [57,58]. Accordingly, the correlation length exponents and corresponding reduced exponents ($\frac{\beta}{\nu}$, $\frac{\gamma}{\nu}$) have been calculated and compared with the well-known theoretical models (Supplemental Material table). The reduced critical parameters do not match with any of the theoretical parameters and there is a possibility of more than one existing correlation length, $\xi(T)$, corresponding to different σ (or ν) in the system (details given in the Supplemental Material). According to the theoretical work on the Griffiths singularity by McCoy [57], a system with immobile random impurity (quenched disorder) exhibits a second length scale corresponding to that impurity. Normally, in polycrystalline compounds, the average grain size is small and the ξ exceeds the grain size, while T approaches close to T_C [43]. Therefore, the fluctuation effects can be ignored and the system follows the mean-field model [43]. However, when the ξ is comparable to the disorder/impurity length scale in the presence of quenched disorder in the system, while the temperature is approaching close to T_C, the effect of a small amount of disorder/impurity might be significant despite the impurity length scale being small compared to the grain size of the compound [57]. This may result in the deviation of critical parameters from usual values. Hence, the presence of an additional critical exponent correlation length scale in the sample substantiates the existing disorder, which may help to appear and stabilize the short-range magnetic interaction or the GP at the above T_C regime in the system [9,57]. Therefore, clearly, the observed unusual critical parameters of the system do not belong to any well-known existing universality classes or weak-universality classes, which, on the other hand, also substantiates the inhomogeneous (magnetic) nature of the system.

The variation of γ value from the mean-field model has also been reported in different systems, e.g., $Zr_{1-x}Nb_xZn_2$ [61], antiperovskite $Cu_{1-x}NMn_{3+x}(0.1 \leqslant x \leqslant 0.4)$ [62], single-crystalline $La_{0.7}Sr_{0.3}MnO_3$ [10], $La_{1-x}Ca_xMnO_3(x = 0.20, 0.21)$ [44] systems, etc. Sokolov *et al.* [61] discussed the deviation of the γ value from the mean-field value in a $Zr_{1-x}Nb_xZn_2$ compound by the originated disorder with Nb substitution in the system. Khan *et al.* [44] explained the obtained high value of γ in single-crystalline $La_{0.79}Sr_{0.21}CoO_3$ system by taking into account the existence of severe critical fluctuations at the $T > T_C$ regime appeared owing to the presence of inhomogeneity in the system. According to Lin *et al.* [62], the existing short-range AFM interaction above the $T > T_C$ region and presence of critical fluctuations in the $Cu_{1-x}NMn_{3+x}$ system are responsible for the deviation in γ value from the mean-field model. Thus, the observed γ value in the nanomaterial reflects a gradual divergence of magnetic susceptibility for $T > T_C$ range that may also be a consequence of existing disorder/defect in the compound as mentioned earlier. On the other hand, the unusually high β value has also been reported in different systems [63]. Butch *et al.* [63] explained the unusual β exponent with considering the presence of fluctuations that appears owing to the disorder of Re substitution in $URu_{2-x}Re_xSi_2$ systems. Cheng *et al.* [64] delineated the estimated abnormal β value in Ca-substituted $Sr_{1-x}Ca_xRuO_3$ compounds due to the strong spin-orbit coupling that results in a phase segregation between weakly correlated and strongly correlated phases. According to Müller-Krumbhaar [42], the presence of lattice inhomogeneity, i.e., introduction of missed spin clusters within a homogeneous Heisenberg spin system, causes enchancement of the β value. Hence, the obtained high value of β indicates the slow growth of ordered moment below T_C and it may be a consequence of having disorder or magnetic inhomogeneity in the present system. Further, the critical exponent, δ, is found to be less than the mean-field model. It is also substantiated from the decreasing curvature of the $M(H)$ isotherms. The critical analysis in single-crystalline doped perovskite manganites have also been carried out by Jiang *et al.* [5,27] and Salamon *et al.* [1,10]. They characterized the GP by unusual critical exponents, particularly, the abnormally large δ value, while arguing if the CMR is a Griffiths singularity or not. However, the obtained unusual critical parameters in the present system differ from their estimated values and, apparently, do not belong to any of the given university classes. The possible origin of this disparity is the different bivalent doping concentrations present in the compound or the intrinsic inhomogeneity that arises due to the polycrystalline nature of the nanomaterial in the microscopic scale and it, ostensibly, depends on the different preparation techniques, as explained by other groups [43,65–67]. Moreover, the deviation of critical values from the usual mean-field model has also been explained with the increase in A-site cationic disorder by Banik *et al.* [48]. Therefore, it may be concluded that the

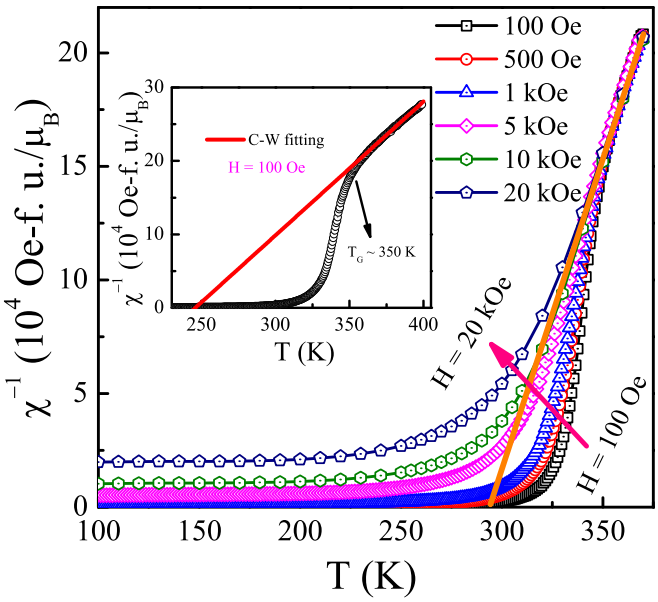

FIG. 5. Inverse magnetic susceptibility as a function of temperature for external magnetic field $H = 100$ Oe, 500 Oe, 1 kOe, 5 kOe, 10 kOe, 20 kOe. Solid line is the guide to eyes to note the deviation. Inset: linear fitting of true PM phase up to 400 K for $H = 100$ Oe.

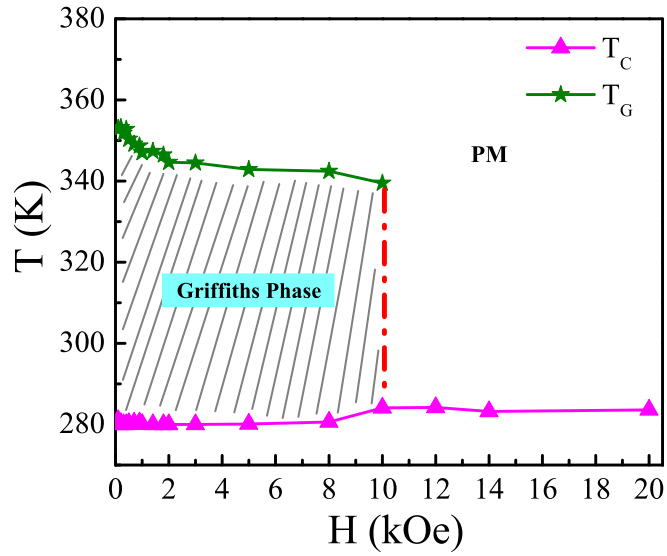

FIG. 6. Phase diagram of H versus T. The shaded region is Griffiths phase region.

intrinsic disorder and magnetic inhomogeneity are present in the LCSMO nanomaterial. The presence of disorder/defect in a system is a prerequisite of appearing the GP in a system as reported in Refs. [8,9]. It is also worthwhile to note that the calculated T_C in critical analysis differs from the observed T_C in dM/dT versus T curve. It is because the Curie temperature $T_C \sim 280$ K has been estimated from the broad minima of the dM/dT curve (Fig. 1). The observed deep (minima) is broadened due to the occurrence of two transitions (spin freezing and FM-like) at the nearby temperatures [45].

As observed from the $M(T)$ plots (Fig. 1) and critical analysis, the magnetic phase transition is not a proper FM and the intrinsic inhomogeneity/disorder is present in the system. As mentioned earlier, the intrinsic inhomogeneity/disorder helps to appear short-range magnetic correlation above T_C [9]. Therefore, to get the information of the high-temperature region while approaching toward magnetic phase transition, the inverse susceptibility [χ^{-1}(T)] curves for the magnetic field variation of $H = 100$ Oe, 500 Oe, 1 kOe, 5 kOe, 10 kOe, and 20 kOe have been plotted in Fig. 5. It shows a prominent magnetic field-dependent downturn, i.e., with increasing applied magnetic field the gradual suppression of χ^{-1}(T) downturn is noticed below a certain temperature while advancing close to phase transition from high temperature PM phase. This type of anomalous behavior in χ^{-1}(T) is considered to be a fingerprint of GP [2,4,5,8,11], where the stairlike pattern (in low H) appears only when the small FM clusters start emerging amidst the PM matrix i.e., the magnetically ordered rare region has a higher susceptibility than that of its PM matrix and eventually merges with the high temperature true PM regime in application of high magnetic field, as described in literature [2,8,68]. Thus, the observed pattern of χ^{-1}(T) in Fig. 5 is similar to the behavior of GP phenomenon, which, however, can be destroyed in application of $H > 10$ kOe, where the downward deviation almost merges with the high-temperature magnetization. This high field behavior might be incorporated with, either the FM clusters getting saturated with increasing magnetic field and/or small FM component getting suppressed under the PM background as the magnetization of PM matrix increases linearly under such a high external magnetic field [2]. The Curie-Weiss (CW) fitting of χ^{-1}(T), under $H = 100$ Oe, has been displayed separately in the inset of Fig. 5. The dependance of χ^{-1}(T) is linear in the high temperature region (i.e., $T > 350$ K to up to 400 K) and follows the CW law well. In this true PM region, the experimentally observed effective PM moment, $\mu_{\text{eff}}^{\text{obs}} = 4.94\,\mu_B$/f.u. almost matches with the theoretical value, $\mu_{\text{eff}}^{\text{theo}} = 4.33\,\mu_B$/f.u. [69]. However, χ^{-1}(T) deviates from the CW behavior around the temperature ~ 350 K (T_G), which is marked as the onset of GP as mentioned earlier. The existence of the GP has also been incorporated with a phase diagram of H versus T shown in Fig. 6. Moreover, the susceptibility obeys the following law, $\chi^{-1}(T) \propto (T\text{-}T_C^R)^{1-\lambda}$ $(0 \leqslant \lambda < 1)$, in the GP region [1,2,5,10], where λ is the magnetic susceptibility exponent and T_C^R is the critical temperature of random FM clusters where the susceptibility diverges. Generally, in this region a singularity (termed as the Griffiths singularity) is observed between the GP and high-temperature PM phases. To identify GP and to distinguish the singularity, the 100 Oe χ^{-1}(T) curve has been plotted again with reduced temperature $t_m = T/T_C^R$ - 1 in log-log scale. Using the aforesaid power law, the λ values for the PM region (λ_{PM}) and the GP region (λ_{GP}) can be easily determined by linear fitting the higher and lower reduced temperature portion of the log-log plot, respectively. The double log plot and the linear fitted data have been shown in Fig. 7. It should be noted that an incorrect value of T_C^R may lead to an unphysical fitting along with an inaccurate value of λ [8,70]. The value of λ_{PM} in the pure PM region is expected to be 0 (zero). On the other hand, the λ_{GP} value will be finite (i.e., between 0 and 1) in the GP region owing to the existing finite-size FM clusters amidst PM matrix above T_C. The

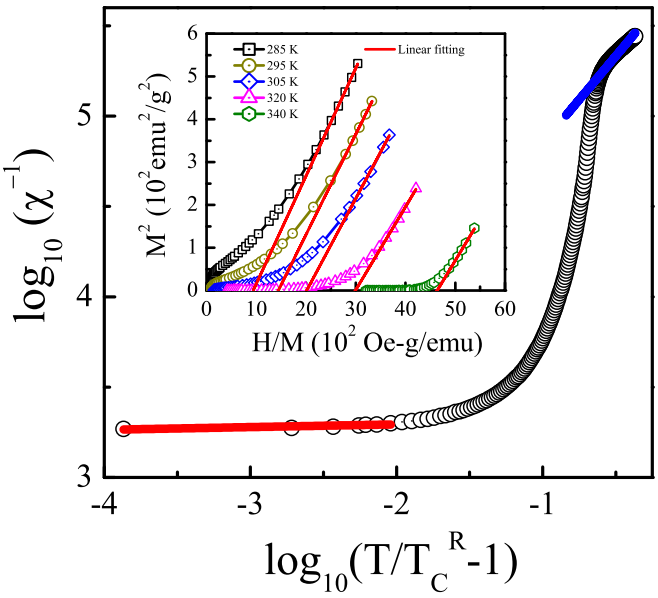

FIG. 7. Double-logarithmic plot of inverse susceptibility against reduced temperature. Solid lines indicate the linear fitting at the GP and PM region. Inset: Arrott plots at the temperatures above T_C. Solid lines are the linear extrapolation from the high field region.

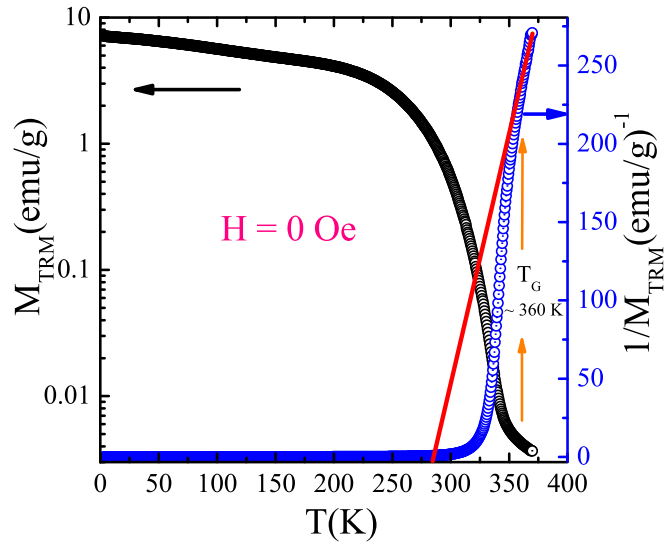

FIG. 8. Thermoremanent magnetization (left axis) and inverse thermoremanent magnetization (right axis) as a function of temperature after cooling down the system at $H = 100$ Oe.

observed values from the fitting are $\lambda_{GP} \sim 0.984$ and $\lambda_{PM} \sim 0.035$, which is very close to zero. It is worthwhile to mention that, in realistic systems, a GP evolves into a conventionally disordered PM phase [5], where a weaker magnetic correlation with very low magnetic moment [71,72] can be observed owing to the existing noninteracting FM clusters (very small in number). Thus, it is difficult to obtain $\lambda_{PM} = 0$ at the PM region for a real system [4,8]. However, this interaction in the PM region is so small that the state can be considered as a pure PM state as given in previous literature [8]. The degree of deviation in χ^{-1}(T) from its high temperature CW behavior and the value of λ_{GP} determine the strength of GP. Hence, the high value of λ_{GP} indicates the presence of a strong GP in the system. Here, strong means the Griffiths singularity is reasonably strong in the system that needs H > 10 kOe to overcome. In a different way, the deviation in χ^{-1}(T) from the CW line is very large and the temperature range of GP normalized with respect to T_C calculated as GP(% T_C) = $[\frac{T_G - T_C}{T_C}] \times 100$ is also high, i.e., $\sim 28\%$ [8]. These λ values are very comparable with other reported manganite materials [71,73] as well as double perovskite systems [16,17]. It should be mentioned that the possibility of diverging the susceptibility before the beginning of long-range ordering at T_C has been taken into consideration by Griffiths in his original work on the GP [9]. Moreover, the chances of the spontaneous magnetization appearing in the temperature regime above T_C have also been predicted by MaCoy, while characterizing Griffiths singularity [57]. Therefore, to discard the possibility of having spontaneous magnetization above T_C in this system, M^2 versus H/M curves (Arrott plot [49]) have been shown for few temperatures in GP regime [*M(H)* curves have been discussed later] in the inset of Fig. 7. The high-field data of these curves have been linearly fit and extrapolated to $H/M = 0$. It intersects on the negative M^2 axis, which implies no spontaneous magnetization as well as long-range FM ordering in that region [2].

As GP phenomenon is restricted in the low field region only, a perturbation like magnetic field is expected to play a significant role on such a localized spin texture. To avoid such circumstances, the thermoremenent magnetization [M_{TRM}(T)] experiment has been employed, where the magnetic measurement is carried out in zero field. In this protocol, the sample is first cooled down to a lower temperature from well above its transition temperature ($T > T_G$) under an applied magnetic field ($H = 100$ Oe for this case) and the field is switched off at the lower temperature. The M_{TRM}(T) is recorded during warming cycle under this zero applied magnetic field. It shows an upturn at the magnetic transition. The GP signature is noticed from the slight upturn in M_{TRM}(T) above the FM-like transition temperature (T_C). It is also substantiated with the observed downturn around that same transition temperature in the inverse thermoremenent magnetization [$1/M_{TRM}$(T)] plot. Both curves have been shown in Fig. 8. The GP transition temperature, T_G is observed around $\sim$ 360 K. Both T_C and T_G are slightly higher than conventional in-field T_C and T_G and signifies the influence of magnetic field in the phase transition. Though such type of measurement protocol has limited utilization to probe piezomagnetism [74], spin-glass [75] etc., it has also been performed previously to explore GP in different systems [68,76].

The existing magnetically ordered rare regions (GP) significantly influence the spin dynamics of the magnetic susceptibility [23]. Hence, the spin dynamics in the GP region are different from the high-temperature PM regime. The dynamic properties are characterized by the average spin autocorrelation function, *C(t)*. In the pure PM range ($T > T_G$), the autocorrelation function is expected to fall exponentially, owing to the absence of any locally ordered rare regions [23,68]. In contrast, in the GP regime ($T_C < T < T_G$), a nonexponential decay of the autocorrelation function is noticed as the required time to flip the effective spin of large magnetically

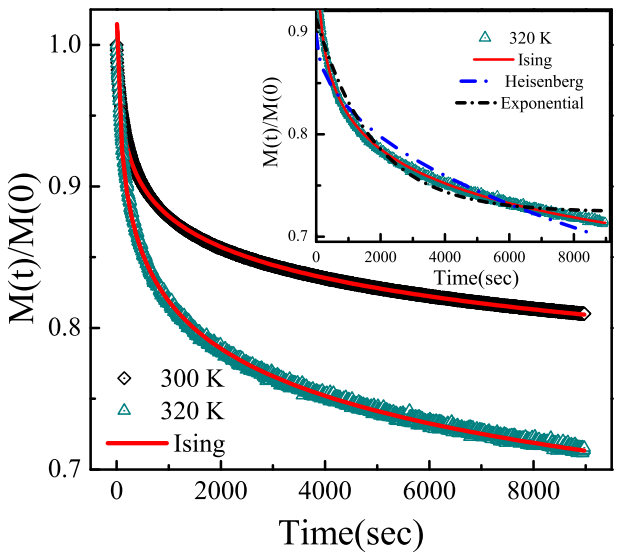

FIG. 9. Isothermal remanent magnetization (IRM) at $T = 300$ K and 320 K along with its Ising fit. Inset: Deviation of exponential as well as Heisenberg fits at $T = 320$ K.

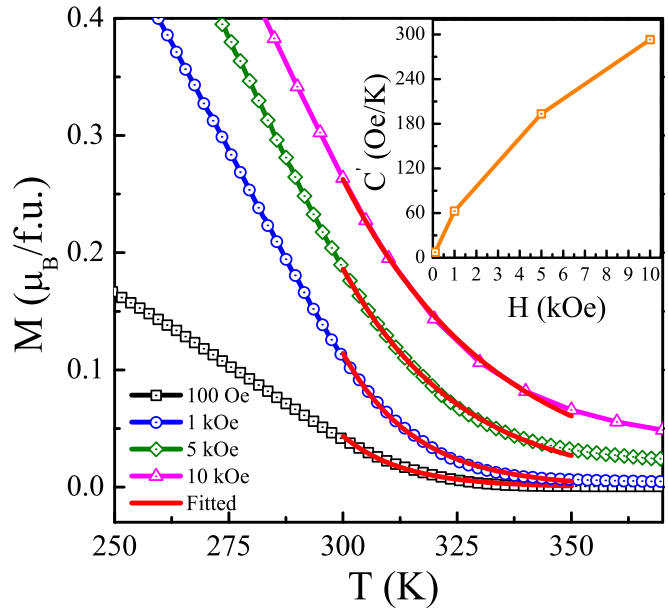

FIG. 10. FCW magnetization data for $H = 100$ Oe, 1 kOe, 5 kOe, and 10 kOe and the corresponding theoretical fitted curves (solid lines) obtained using the model proposed by Galitski *et al.* [Eq. (10)] at the Griffiths phase region. Inset: The estimated constants in Eq. (10) as a function of magnetic field (in kOe) plot.

ordered regions is high, which apparently slows down the dynamics [23,68]. The slowing down can be manifested in the form of a power law in the magnetic relaxation measurement, i.e., the magnetization decay as a function of time. This slowing down of the dynamics of the system is regarded as a prerequisite for a GP [23]. To incorporate that, the isothermal remanent magnetization (IRM) measurement for the LCSMO compound has been carried out within the GP regime. The decay has been characterized as $C(t) \sim \exp[-A(\ln t)^{d/d-1}]$ for Ising spin systems and $C(t) \sim \exp[-Bt^{0.5}]$ for Heisenberg spin systems [23]. The system was cooled from $T = 380$ K to the desired temperatures, i.e., $T = 300$ K and 320 K at an applied magnetic field, $H = 500$ Oe and the decay of magnetization was measured as a function of time after sudden removal of the magnetic field. The IRM data implies that the decay perfectly follows the functional form of the Ising spin systems discussed previously. The experimental and fitted data have been shown in Fig. 9. The deviation from the functional form of exponential and the Heisenberg systems (at $T = 320$ K) has also been shown in the inset of Fig. 9. Thus, it indicates that the observed state above T_C for the system is not a pure PM state, rather a GP exists that slows down the spin dynamics. In the earlier reported results, a Heisenberg-like spin interaction in the magnetization decay was observed [68,77], however, in contrast to that, the Ising spin interaction is noticed in the present system. This observed Ising spin interaction in the present compound has been incorporated in the aforementioned critical analysis section.

As formerly stated, the disorder in a system is considered to be the prerequisite in the GP appearing [9]. To identify and confirm the presence of the GP associated with disorder in the system, the *M(T)* curves at $H = 100$ Oe, 1 kOe, 5 kOe, and 10 kOe for the temperature region of 300 K to 350 K have been fitted with the model (shown in Fig. 10) proposed by Galitski *et al.* in their theoretical study on role of disorder in the GP [78]. According to it, the magnetization under magnetic field in GP region obeys the following formula:

$$M(T, H) \propto \exp[-C'(T/H)]. \tag{10}$$

$C' = k_B/\mu_{\text{ave}}$ is constant, k_B stands for Boltzmann constant, and μ_{ave} indicates the average magnetic moment of FM clusters in the GP. Therefore, C' is inversely proportional to μ_{ave}. We have shown in Fig. 10 that, in the GP regime, *M(T)* curves would be perfectly described by the above model. The enhancement in the estimated C' value with increasing applied magnetic field (inset of Fig. 10) indicates the drop in the average magnetic moment of FM clusters. Hence, it evidences the presence of the GP in the system that starts disappearing upon application of large magnetic field due to the increase in magnetization of the PM background. It matches with our aforementioned observation. In addition, the average size (diameter) of the FM cluster can also be estimated utilizing the above expression. Only the $H = 100$ Oe *M(T)* fitting parameter (μ_{ave}) has been taken into consideration for calculation to avoid the unwanted PM contribution to the magnetic moment. Considering the saturation magnetization of one formula unit is $3.4\,\mu_B$ and the observed $\mu_{\text{ave}} \simeq 2 \times 10^3\ \mu_B$, the average diameter of FM clusters comes out to be ~ 6.5 nm, which is comparable to the other reported values [79,80]. In addition, it may also be concluded that the existing disorder, originating due to the mismatch of different elements at the A-site as well as the formation of nanograins in the system, helps to grow the GP in the system.

B. Isothermal magnetization

As discussed earlier, the region above T_C is not purely PM for this system. The presence of GP can also be distinguished via analyzing magnetic isotherms [*M(H)*]. These isotherms

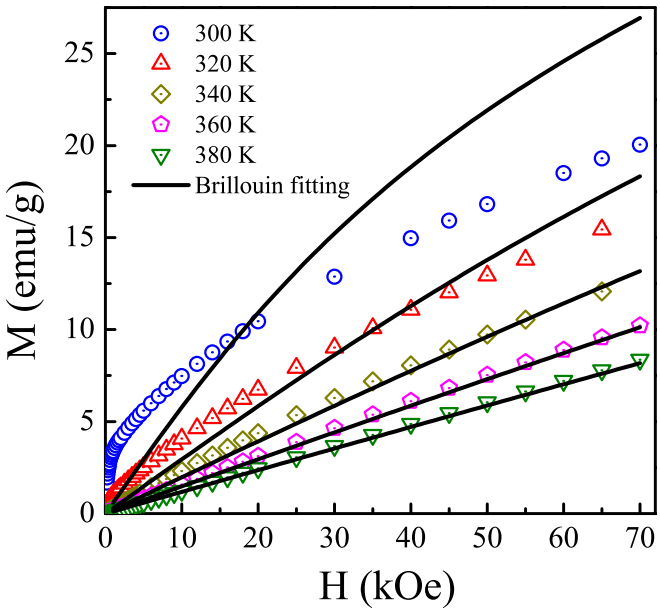

FIG. 11. *M(H)* isotherms at different temperatures for the region $T > T_C$. Solid lines are the corresponding simulation curves generated using Brillouin function.

have been recorded in ZFC mode at constant temperatures. The magnetization value of experimentally observed first quadrant *M(H)* isotherms (above T_C) reduces with increasing temperature and increases with increasing magnetic field. This indicates the absence of any long-range magnetic ordering in this region [81]. However, a rise in magnetization in the lower field region (particularly, for $T = 300$ K) has been noticed that also reduces with increasing temperature. It may appear due to the presence of short-range FM ordering. Thus, to get deeper understanding, these *M(H)* isotherms have been compared with the theoretically simulated *M(H)* curves. The theoretical *M(H)* curves have been obtained using Brillouin function $B_J(x)$ assuming the system exhibits a true PM behavior above T_C [81]. Hence, the magnetization can be written as

$$M_{\text{theo}}(H) = NgJ\mu_B B_J(x), \tag{11}$$

with $x = gJ\mu_B H/k_B T$. Here, N is the number density of Mn^{3+}/Mn^{4+} ions or magnetic dipoles, g stands for Landé g factor, J is the total angular momentum of Mn^{3+}/Mn^{4+} ions (here, $J = 0.4 \times 2 + 0.6 \times 3/2 = 1.7$), μ_B and k_B stand for Bohr magneton and Boltzmann constant, respectively. Both the simulated and experimentally observed curves have been plotted and compared in Fig. 11. It is seen that the simulated curve excellently follows the experimental curve for the temperatures above T_G (i.e., $T = 360$ K and 380 K), but does not match well for the temperatures $T_C < T < T_G$. At $T = 300$ K, the experimental magnetization value is higher (lower) in the low- (high-) field region with respect to the theoretically calculated values. This may be an indication of complex microscopic arrangement with FM and AFM/glassy/frustrated regions at the GP state. This ambiguity can easily be explained considering the scenario of FM clusters, being squashed in the PM matrix, as analogous to FM/PM/FM trilayer thin films with FM regions having directional anisotropy [82]. The embedded nano FM cluster formation in the PM region can also be considered as core-shell type [76], where the core comprises with FM entity and the shell contains frustrated/glassy regions. However, it should not be confused with the nanomaterial's core-shell structure. In this scenario, the FM spins at the core try to orient along the magnetic field direction along with the shell frustrated/glassy regions at the low field regime and the magnetization increases with magnetic field. In this situation, the FM-cluster-phase contributes broadly to the total magnetization with respect to the global PM matrix and as a consequence, magnetization increases compared to theoretical value at the low field region. On the other hand, when the increase in magnetic field crosses the critical field of the GP (i.e., H > 10 kOe), the nano FM clusters get magnetically saturated and, owing to an increase in polarization of spins in the PM matrix, FM cluster contributions are masked under the PM matrix. Thus, the average moment of FM clusters decreases, as shown previously in the inset of Fig. 10. However, due to the existent magnetic anisotropy of FM clusters, they are ordered in different ways. Thus, the outer shell spins of these clusters are orientated as magnetically disordered because of the increase in the FM proximity effect toward the peripheral area of clusters with increasing magnetic field [82]. As a result, magnetization at the high-field region decreases compared to theoretical value. Additionally, it may also be concluded that the considerable difference between the simulated and experimental curves at the high- as well as low-field regions at $T = 300$ K apparently evidences the presence of a large number of FM clusters amidst the PM matrix. However, the difference of the higher and lower field regions starts suppressing with increasing temperature as the interactions of FM clusters are diluted with increasing temperature. It may also be noted that the simulation data for $T = 340$ K overlaps partially with the experimental curve and, perhaps, it is an indication of disappearing the GP and emergence of true PM phase as the temperature is approaching close to T_G. Hence, the system does not show a pure PM behavior below T_G.

To see the magnetic behavior in the low-field region, the derivative of initial magnetization (dM_i/dH) with respect to magnetic field at different temperatures has been plotted in Fig. 12. The curves at $T = 220$ K and 260 K show a discernible peak in the low-field region and up to $T \sim T_C$, it shifts toward an even lower field region with increasing temperature. This kind of behavior is expected in a FM system [83]. However, the peak disappears for temperatures above T_C and, interestingly, the raise in the curve at the low-field region persists up to $\sim T_G$. Above that, for $T = 360$ K and 370 K, linear behavior is observed. Hence, the uprise in dM_i/dH may be a consequence of existing GP in the temperature range $T_C < T < T_G$. Additionally, it was predicted by Wortist [84] and by Harris [85] in their theoretical calculations on GP that all the magnetization derivatives with respect to field (i.e., dM/dH) above T_C are finite at $H = 0$ for a GP system. Hence, the observed upraise at the lower field region for the temperature range $T_C < T < T_G$ in Fig. 12 supports the theoretical prediction.

It has been previously mentioned that GP appears due to the formation of FM clusters in the PM phase. Hence, to investigate it along with its interactions properly, *M(H)* isotherms at different temperatures have been investigated again. Magnetic isotherms are generally expressed with the Langevin

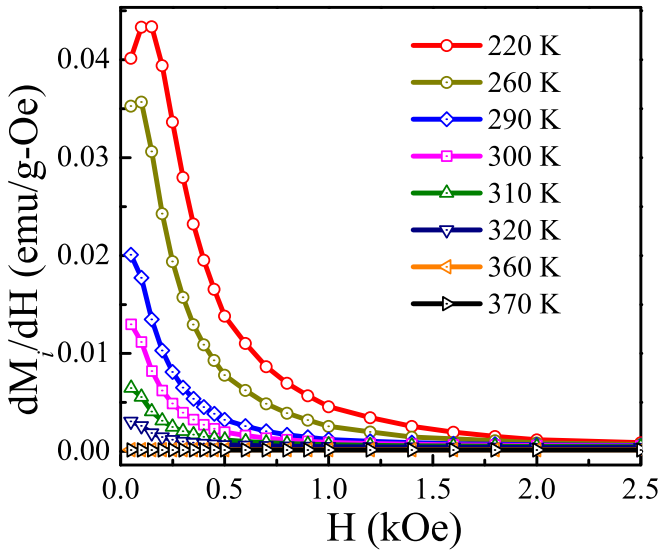

FIG. 12. dM_i/dH (M_i is initial magnetization) versus H at different temperatures both below and above T_C.

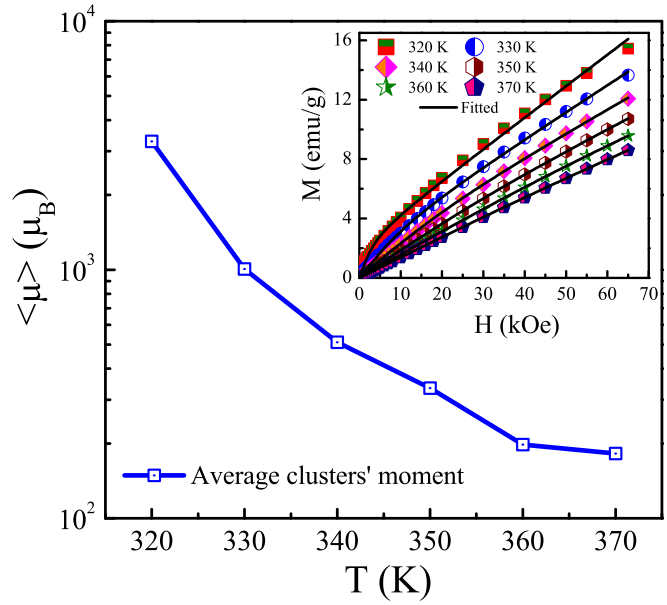

FIG. 13. Average clusters' moment as a function of temperature for GP regime ($T = 320$ K, 330 K, 340 K, 350 K, 360 K, and 370 K). Inset: Isothermal magnetization at different temperatures in the $T > T_C$ region. Solid lines are the corresponding modified Langevin fitted curves.

equation for a true PM material [86,87]. However, isothermal magnetization for a system with existing FM clusters amidst the PM background follows a modified Langevin function [71,88]. According to this model, the $M(H)$ can be written as

$$M(H) = N < \mu > L\left(\frac{< \mu > H}{k_B T}\right) + AH. \qquad (12)$$

Here N is the FM cluster density in the PM region, $< \mu >$ is average magnetic moment of the clusters; $[L(x)]$ denotes the Langevin function with $x = \frac{<\mu>H}{k_B T}$; k_B, H and T are, respectively, Boltzmann constant, applied magnetic field, and temperature. Here, the A term is added in the standard Langevin function to incorporate the linear magnetization fraction with magnetic field. Using this relationship, the $M(H)$ isotherms for different temperatures ($T > T_C$) have been fitted (inset Fig. 13). Utilizing the fitting parameters, $< \mu >$ has also been estimated and plotted as a function of T (shown in Fig. 13). It is noted that the average magnetic moment is high at the GP region. However, it starts reducing from the GP region to the above T_G with increasing temperature owing to the enhancement of the PM matrix. The high value of magnetic moment at the GP region implies the clustering of few atomic spins. Assuming the cluster's shape is spherical and taking the average cluster moment of one formula unit is 3.4 μ_B with volume 243.15(3) Å^3 (unit cell volume), the size (diameter) of these clusters has been estimated. The approximate diameter of the cluster at $T = 320$ K comes out to be $\sim$ 7.6 nm. However, the diameter is greater than the value estimated using Eq. (10). This disagreement may have emerged from the substantial PM contribution to the magnetic moment due to the strong magnetic field variation of $H =$ 65 kOe.

On the other hand, it is well established that, when the particle size reaches the nanometer scale, it may behave like superparamagnetic materials, i.e., it acts like an individual FM entity [89–91]. Thus, to discard the appearance of superparamagnetic phase associated with this existing FM clusters at $T > T_C$, normalized magnetization (M/M_s) versus H/T has been plotted at different temperatures ($T_C < T < T_G$) and is shown in Fig. 14. These curves collapse onto a single curve if clusters are superparamagnetic [91]. However, the diverting nature of each isotherm from another discards the presence of a superparamagnetic phase of the nanoparticle in the temperature region $T_C < T < T_G$.

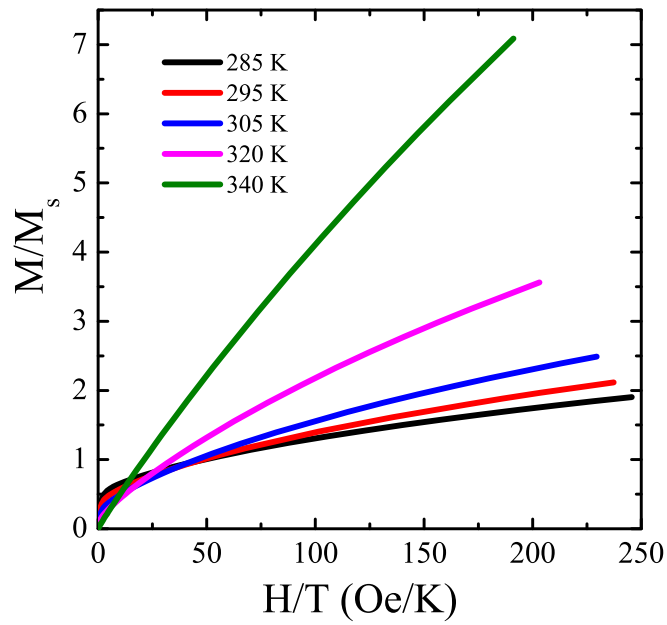

FIG. 14. M/M_S (Normalized magnetization) versus H/T plots for the temperature regime $T_C < T < T_G$.

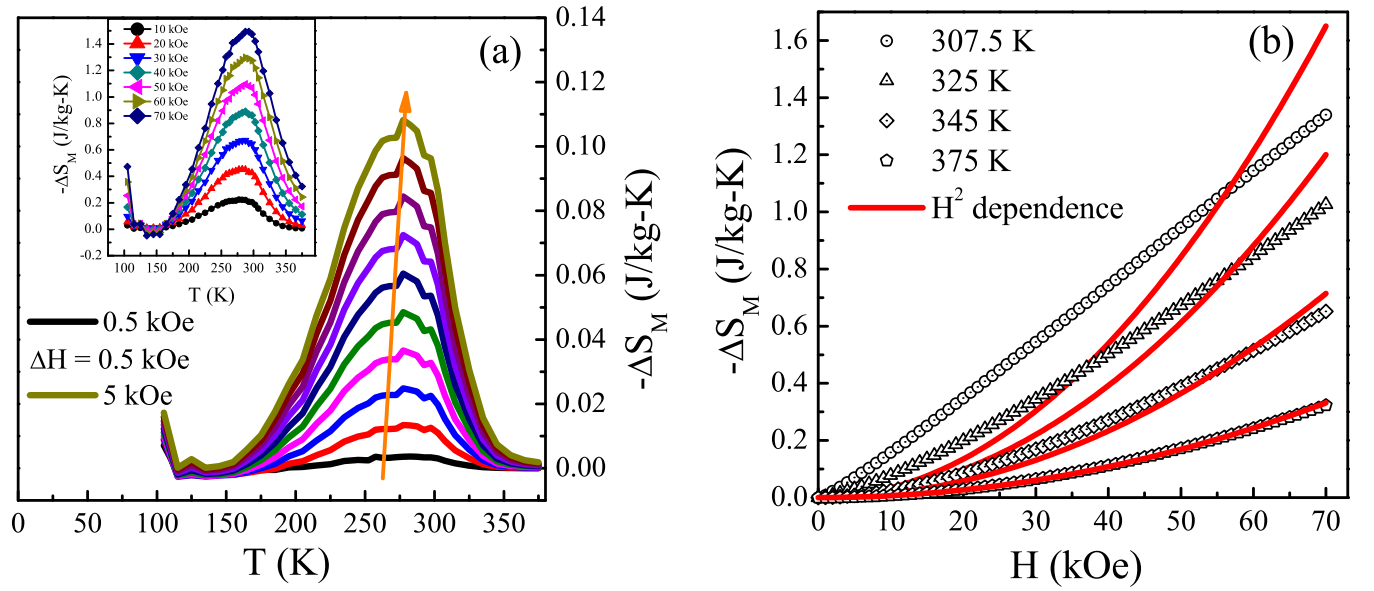

FIG. 15. (a) Negative magnetic entropy change ($-\Delta S_M$) as a function of temperature at various low applied magnetic field changes (0.5 to 5 kOe). Inset: $-\Delta S_M$ versus T at higher applied magnetic field variation. Continuous lines are for guide to the eyes. (b) $-\Delta S_M$ as a function of applied magnetic fields at various constant temperatures in the regime $T > T_C$. Solid lines are the H^2 dependance curves.

C. Magnetocaloric effect

The MCE in a material is largely used to achieve magnetic refrigerations [92,93]. This MCE of a system is the output of magnetic entropy change that arises owing to the coupling of associated magnetic spins in presence of applied magnetic field, i.e., in application of magnetic field, the spins orient along the field and helps to reduce the total magnetic entropy of the system. Hence, the magnetic entropy change is related to magnetic spins and depends on magnetic field strongly. Therefore, it is worthwhile to mention that, to probe the short-range magnetic interaction in a material, MCE is a powerful tool to utilize. It is also well reported that the presence of short-range magnetic interaction in PM region hinders the maximum magnetic entropy change at the magnetic transition temperature, i.e., it does not allow us to achieve maximum magnetic entropy change as predicted by theoretical calculations [94,95]. Thus, to comprehend GP more precisely, MCE analysis has been performed. The MCE is calculated from magnetic isotherms using the following Maxwell's thermodynamic relation: $\Delta S_M = \int_0^H (\frac{\partial M}{\partial T})\, dH$. The observed entropy change is 1.49 J/Kg-K for a magnetic field change of 0–70 kOe. To understand it rigorously, the ΔS_M has been plotted as a function of temperature for different magnetic field variation. From Fig. 15(a), the broad hump as well as the asymmetrical distribution of ΔS_M values around its maximum value (i.e., around T_C) is clearly noticed for the low field (i.e., up to 5 kOe) MCE plots. In the inset of Fig. 15(a), it has been compared with the $H = 10$ kOe ΔS_M curve with other high field plots. Interestingly, the asymmetrical nature and broadness of humps start reducing with increasing magnetic field, particularly for $H > 10$ kOe. In general, a system with long-range ordering exhibits a symmetrical temperature evolution of ΔS_M. On the other hand, asymmetry is noticed in a system that incorporates short-range ordering [96,97]. However, theoretically in the PM regime, $\Delta S_M \sim H^2/2T^2$, here H and T are, respectively, the applied magnetic field and the corresponding temperature [97]. Hence, at a constant temperature, $\Delta S_M(H) \propto H^2$. The experimental and fitted $\Delta S_M(H)$ curves at the above T_C regime have been shown in Fig. 15(b). The best H^2 dependence is noticed above T_G. It implies that the true PM region exists above T_G. It is also consistent with the previously observed linear behavior of χ^{-1}(T) curve and best fitted *M(H)* curves using the Brillouin function above T_G. However, in the temperature region $T_C < T < T_G$, $\Delta S_M(H)$ does not show H^2 dependance, which indicates that short-range interaction persists in this regime. It is worth mentioning here that the linear increase on $-\Delta S_M$ in Fig. 15(b) is because the saturation field was still not achieved, as observed in Fig. 3(d). Thus, the existence of short-range interaction may be the reason of getting a magnetic entropy change over a broad temperature range [in Fig. 15(a)] up to the field variation, $H = 10$ kOe, as the GP exists up to that field. For $H > 10$ kOe, GP vanishes and, with increasing magnetic field, asymmetry in the ΔS_M(T) decreases.

To get profound evidence about the short-range FM interaction or FM clustering at the above T_C regime, the theoretical magnetic entropy relation derived from the mean-field theory has been taken into consideration. This formula was established by taking into account the relation between magnetization and magnetic entropy and it has also been previously utilized to various systems including manganite compounds to probe the effect of short-range magnetic interaction on magnetic entropy [94,95]. But, in the present paper, it has been used to investigate the existence of GP. Therefore, the GP regime of ΔS_M versus T curves has been fitted with the following relation:

$$\Delta S = -Nk_B\left[\ln(2J+1) - \ln\left(\frac{\sinh(2J+1)x/2J}{\sinh(x/2J)}\right) + x\Delta\sigma\right]. \quad (13)$$

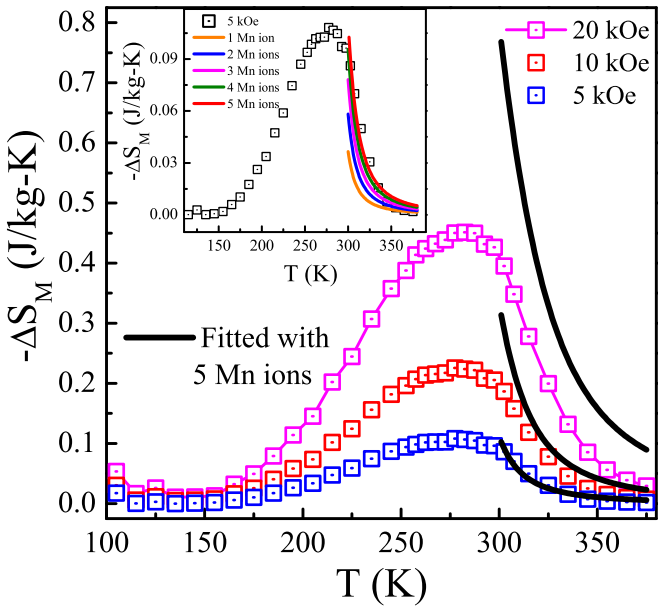

FIG. 16. Magnetic entropy change as function of temperature for applied magnetic field variation of 5 kOe, 10 kOe, and 20 kOe. Dotted hollow squares are the experimentally observed data and solid lines are the corresponding simulation curves obtained using Eq. (13) with $m = 5$ Mn ions for $T > T_C$ region. Continuous line for 20 kOe data is the guide to eyes. Inset: Theoretically generated data using Eq. (13) with $m = 1$ to 5 Mn ions and fitted with ΔS_M versus T curve for 0 to 5 kOe field variation at $T > T_C$ regime.

$\Delta\sigma$ stands for the normalized magnetization change and is derived from $\Delta\sigma = \sigma\text{-}0 = B_J(\mathrm{x})$; where $B_J(x)$ stands for the Brillouin function with $x = gJ\mu_B(H + \lambda\sigma)/k_BT$, other symbols have been described earlier in Eq. (11). Assuming that the short-range FM interaction appears due to the presence of more than one Mn ion in the clusters, the above T_C regime has been fitted using the aforementioned equation by replacing N and J, respectively, with N/m and mJ, where m is the number of Mn ions in the FM clusters. Considering five Mn ions in the clusters, the theoretical model follows the experimental MCE curves satisfactorily in the GP region for the field variations of 5 kOe and 10 kOe (Fig. 16), but it does not follow the experimental curves above $H = 10$ kOe. Further, to clarify, the 5 kOe MCE curve has been again fitted with taking m values from 1 to 5 and shown in the inset of Fig. 16. It is observed that, except the simulation with $m = 5$, none of the theoretical data matches the experimental curve in the GP region. Hence, GP appears in the $T_C < T < T_G$ regime because of the FM clustering and these clusters are composed of at least five Mn ions.

In strongly correlated systems like doped perovskite manganites, the structure and magnetic properties are closely associated and the magnetic inhomogeneity originates owing to bringing in disorder in the system [31]. It arises primarily because of the enhancement in σ^2 in the bulk LCSMO system that creates chemical pressure at the A site, resulting the deviation in the Mn–O–Mn bond angle and Mn–O bond length and, subsequently, the disorder is further increased by reducing its particle size, i.e., nanomaterial (core-shell structure) [45]. Thus, it influences the magnetic properties as the double-exchange/superexchange interactions are strongly dependent on this bond lengths and bond angles. As a result of surface pressure effect in nanocrystal, the Mn–O bond length decreases, which is also responsible for the second-order magnetic phase transition in the system. Moreover, from the pioneering work of Zhang *et al.*, the intergrain barrier between the grains in nanomaterial is considered to be the defect, which hampers the long-range ordering [32]. According to them, for broad FM-like transitions, the double-exchange interaction takes place when the intergrain distance is very small and the atoms are located at the edges of two adjacent grains. Thus, the grains either overlap partially to make Mn–O–Mn chains or the adjacent Mn^+ ion and O^- ions form the Mn–O–Mn bridge to fulfill the criterion of DE interaction. Therefore, if the defect increases, the intergrain distance increases and consequently hinders the long-range ordering. Hence, in this present system, the true long-range magnetic ordering has also been hindered due to the intergrain boundary effect.

It is already described that, the LCSMO nanomaterial forms a core-shell structure, where the core is comprised with FM clusters amidst the AFM matrix and uncompensated spins are located at the shell/surface [45]. It has been delved further to understand the influence of the surface pressure effect on size reduction that acts as a driving force for the GP to emerge in the system. It is useful to consider the surface pressure in nanocrystalline acts as if the material is under high hydrostatic pressure [98,99]. As a result, the structural distortion as well as the strain field is developed in the system. The pressure is given by $P_s = 2S/d$, where S and d denote the surface tension of the material and the diameter of the particle, respectively, and here it is assumed that the nanoparticles are in spherical shape. Thus, the surface pressure increases with decreasing particle size and naturally it produces a high surface pressure for smaller particle sizes [98,99]. To get the rough estimation of P_s, S (≈ 50 N/m) of perovskite oxide titanates has been taken into consideration in this calculation. The estimated pressure that acts on the system of average crystallite size, $d \sim 34$ nm, is ~ 3 GPa. Accordingly, the energy involved for the 2.9% compaction of unit cell of nanomaterial from the bulk is ~ 54 meV. The average crystallite size and the volume of the bulk compound have been taken from Ref. [45]. Thus, the distortion in the structure is developed (as mentioned earlier) and it can be estimated by using the equations in plane (*ab* plane) $\mathrm{OS}_{\parallel} = \frac{2(b-a)}{(b+a)}$ and out-of-plane (along *c* axis) $\mathrm{OS}_{\perp} = \frac{2(a+b-c/\sqrt{2})}{(a+b+c/\sqrt{2})}$ for $a < c/\sqrt{2} < b$. Where, a, b, and c are lattice parameters. The calculated orthorhombic distortions, i.e., strain field parameters at $T = 300$ K ($T_C < T < T_G$) are $\mathrm{OS}_{\parallel} \sim 0.102 \pm 0.004$ and $\mathrm{OS}_{\perp} \sim 0.710 \pm 0.006$. The presence of strain fields in such type of nanomaterials ruffles the Mn–O–Mn network [100] and the small difference between in-plane ($\mathrm{OS}_{\parallel}$) and out-of-plane ($\mathrm{OS}_{\perp}$) strain fields tries to freeze the small FM clusters in the core [100].

Thus, the surface spins are immediately positioned abruptly for $T > T_C$ while the system undergoes a FM-like transition. However, due to the existing surface pressure effect, disorder/grain boundary defects and magnetic inhomogeneity, the small core FM clusters (each contains a few Mn ions only) are pinned in such a way that it gives rise to different exchange interactions as discussed earlier. As these

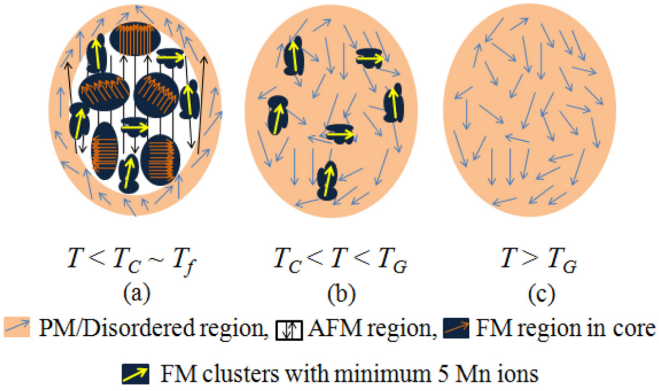

FIG. 17. Core-shell type structure. (a) Shell: Filled with disordered surface spins. Core: FM regions including broken FM clusters (small) having at least five Mn ions in each cluster are embedded amidst AFM background. (b) Broken FM clusters (small) having at least five Mn ions in each cluster in PM matrix. (cluster sizes are not in scale). (c) Complete PM/disordered state.

spins are ordered locally, it forms local regions with large susceptibilities. However, the ordering is not a long-range one [10]. As a consequence of this combined effect, the FM clusters are strengthened and result in the formation of GP. Thus, these clusters cannot reach the PM state entirely just above the T_C due to insufficient thermal energy [32,101,102] and, consequently, short-range FM interaction is observed above the T_C region. With further increasing temperature, these clusters also get sufficient energy to overcome the pinned potential barrier and above T_G a true PM phase is observed. A phenomenological depiction of FM clusters for $T < T_C$ and $T > T_C$ has been given based on the aforementioned statement in Fig. 17 for better understanding. In the diagram, FM regions are embedded in the core AFM matrix with shell uncompensated spins for the $T < T_C \sim T_f$ regime [Fig. 17(a)]. It is worthwhile to mention that the system exhibits a long-range FM-like ordering below T_C ($\sim$ 274 K) to up to $T_f \sim$ 235 K, however, below the temperature 235 K (T_f), the AFM interaction starts ordering and, consequently, glassy magnetic phase is observed below that temperature [45]. The small FM clusters that are pinned with at least five Mn ions (each cluster) in the PM background matrix for the range $T_C < T < T_G$ [Fig. 17(b)]. Finally, the true PM state above $T > T_G$ region [Fig. 17(c)] is observed as the system achieves adequate thermal fluctuation.

The stabilization of GP in the PM regime can also be well explained by using a schematic energy diagram shown in Fig. 18. It primarily incorporates with two local minima (i.e., FM and AFM) for the $T < T_C \sim T_f$ regime [Fig. 18(a)] as the ground state of the system is a glassy-type state. The energy of the pinned clusters are termed as short-range FM (SR FM) potential. Hence, the stability of GP is described with pinning potential barrier (U) in the $T_C < T < T_G$ regime [Fig. 18(b)]. The only way to overcome the barrier is to supply sufficient thermal energy. Thus, above a certain critical temperature (here, T_G), the pinned clusters of the system acquire adequate thermal fluctuations and the whole system reaches a true PM state [Fig. 18(c)] as described in *M(T)* and *M(H)* plots. The pinning potential barrier can be easily calculated

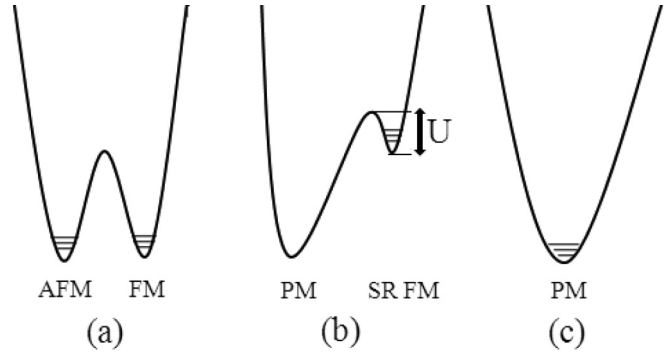

FIG. 18. (a) Two local minima for FM and AFM phase in $T < T_C \sim T_f$ regime. (b) Pinning potential barrier for short-range FM interaction along with PM state in $T_C < T < T_G$ regime. (c) PM state for $T > T_G$ regime.

with U $\sim k_B T$. Where, k_B corresponds Boltzmann constant and T is critical temperature ($\sim T_G$). The value comes out to be $\sim$ 30 meV for the present system. The calculated magnetic energy (E_{mag}) owing to the formation of FM clusters in the GP region for the application of H = 10 kOe is $\sim$ 3 meV. Therefore, $E_{mag} <$ U, but the energy involved for the surface pressure ($\sim$ 54 meV) is high. Thus, the FM clusters get pinned in the system and it needs $\sim$ 30 meV thermal energy to reach to the pure PM region. Hence, the existing strain fields due to the surface pressure effect at the GP region can be the source, which prevents the FM clusters to reach to the PM state immediately above the T_C. Thus, the energy diagram explains well the origin of GP as well as its stability in the PM region in LCSMO system.

IV. CONCLUSION

In conclusion, the presence and origin of GP in $La_{0.4}(Ca_{0.5}Sr_{0.5})_{0.6}MnO_3$ nanomaterial have been studied. The onset of the GP and a FM-like ordering have been observed in the system below $\sim$ 350 K (T_G) and $\sim$ 274 K (T_C), respectively. The GP consisting of short-range FM interaction persists in the temperature region $T_C < T < T_G$. On the basis of different experimental observations and corresponding theoretical analysis based on different proposed models, we have shown that the strain field that developed due to the surface pressure effect and grain boundary defects of the core-shell structure plays a pivotal role to grow and stabilize the GP in nanomaterial. The intrinsic inhomogeneity originated owing to the disorder at the A site and the formation of grain boundary defects in the nanomaterial are the key factors for appearance of the GP. Moreover, the effect of the GP on the magnetic phase transition has also been substantiated by the critical analysis. The comprehensive study presented in this paper is expected to play a key role in understanding the origin of GP in nanomaterials and its correlation with magnetic phase transitions in such systems.

ACKNOWLEDGMENTS

The work was funded by the Department of Atomic Energy (DAE), Government of India, and has been performed at SINP. Suvayan Saha would like to acknowledge DST

(Department of Science and Technology), Government of India, for the INSPIRE fellowship. The authors wish to thank Dr. Santanu Pakhira of AMES Laboratory (Iowa State University, USA) for helpful discussions. The authors also acknowledge Mr. Indranil Mukherjee of IISER Kolkata for helpful discussions on critical analysis.

[1] M. B. Salamon, P. Lin, and S. H. Chun, Phys. Rev. Lett. **88**, 197203 (2002).
[2] P. Tong, B. Kim, D. Kwon, T. Qian, S.-I. Lee, S.-W. Cheong, and B. G. Kim, Phys. Rev. B **77**, 184432 (2008).
[3] A. H. Castro Neto, G. Castilla, and B. A. Jones, Phys. Rev. Lett. **81**, 3531 (1998).
[4] C. Magen, P. A. Algarabel, L. Morellon, J. P. Araújo, C. Ritter, M. R. Ibarra, A. M. Pereira, and J. B. Sousa, Phys. Rev. Lett. **96**, 167201 (2006).
[5] W. Jiang, X. Z. Zhou, G. Williams, Y. Mukovskii, and K. Glazyrin, Phys. Rev. B **77**, 064424 (2008).
[6] A. Ślebarski, J. Goraus, and M. Fijałkowski, Phys. Rev. B **84**, 075154 (2011).
[7] K. Ghosh, C. Mazumdar, R. Ranganathan, S. Mukherjee, and M. De Raychaudhury, Phys. Rev. B **98**, 184419 (2018).
[8] A. K. Pramanik and A. Banerjee, Phys. Rev. B **81**, 024431 (2010).
[9] R. B. Griffiths, Phys. Rev. Lett. **23**, 17 (1969).
[10] M. B. Salamon and S. H. Chun, Phys. Rev. B **68**, 014411 (2003).
[11] J. Deisenhofer, D. Braak, H. A. Krug von Nidda, J. Hemberger, R. M. Eremina, V. A. Ivanshin, A. M. Balbashov, G. Jug, A. Loidl, T. Kimura, and Y. Tokura, Phys. Rev. Lett. **95**, 257202 (2005).
[12] C. L. Lu, X. Chen, S. Dong, K. F. Wang, H. L. Cai, J.-M. Liu, D. Li, and Z. D. Zhang, Phys. Rev. B **79**, 245105 (2009).
[13] T. Qian, P. Tong, B. Kim, S.-I. Lee, N. Shin, S. Park, and B. G. Kim, Phys. Rev. B **77**, 094423 (2008).
[14] R.-F. Yang, Y. Sun, W. He, Q.-A. Li, and Z.-H. Cheng, Appl. Phys. Lett. **90**, 032502 (2007).
[15] Y. Shimada, S. Miyasaka, R. Kumai, and Y. Tokura, Phys. Rev. B **73**, 134424 (2006).
[16] H. S. Nair, D. Swain, S. Adiga, C. Narayana, and S. Elzabeth, J. Appl. Phys. **110**, 123919 (2011).
[17] W. Liu, L. Shi, S. Zhou, J. Zhao, Y. Li, and Y. Guo, J. Appl. Phys. **116**, 193901 (2014).
[18] A. K. Singh, P. Balasubramanian, A. Singh, M. Gupta, and R. Chandra, J. Phys.: Condens. Matter **30**, 355401 (2018).
[19] A. M. Pereira, L. Morellon, C. Magen, J. Ventura, P. A. Algarabel, M. R. Ibarra, J. B. Sousa, and J. P. Araújo, Phys. Rev. B **82**, 172406 (2010).
[20] P. Moretti and M. A. Munoz, Nat. Commun. **4**, 2521 (2013).
[21] R. Yamamoto, T. Furukawa, K. Miyagawa, T. Sasaki, K. Kanoda, and T. Itou, Phys. Rev. Lett. **124**, 046404 (2020).
[22] I. F. Mello, L. Squillante, G. O. Gomes, A. C. Seridonio, and M. de Souza, J. Appl. Phys. **128**, 225102 (2020).
[23] T. Vojta, J. Phys. A: Math. Gen. **39**, R143 (2006).
[24] S. Ubaid-Kassis, T. Vojta, and A. Schroeder, Phys. Rev. Lett. **104**, 066402 (2010).
[25] D. Nozadze and T. Vojta, Phys. Rev. B **85**, 174202 (2012).
[26] P. Swain, S. K. Srivastava, and S. K. Srivastava, Sci. Rep. **7**, 1223 (2017).
[27] W. Jiang, X. Z. Zhou, G. Williams, Y. Mukovskii, and K. Glazyrin, Phys. Rev. Lett. **99**, 177203 (2007).
[28] A. Karmakar, S. Majumdar, S. Kundu, T. Nath, and S. Giri, J. Phys.: Condens. Matter **25**, 066006 (2013).
[29] C. T. Chen, B. N. Lin, Y.-Y. Hsu, J. D. Liao, W. H. Cheng, C. Y. Lin, H. C. Ku, J. F. Lee, L. Y. Jang, and D. G. Liu, Phys. Rev. B **67**, 214424 (2003).
[30] N. Rama, M. R. Rao, V. Sankaranarayanan, P. Majewski, S. Gepraegs, M. Opel, and R. Gross, Phys. Rev. B **70**, 224424 (2004).
[31] S. Saha, K. Das, S. Bandyopadhyay, and I. Das, J. Magn. Magn. Mater. **460**, 165 (2018).
[32] N. Zhang, W. Ding, W. Zhong, D. Xing, and Y. Du, Phys. Rev. B **56**, 8138 (1997).
[33] L. Balcells, J. Fontcuberta, B. Martinez, and X. Obradors, Phys. Rev. B **58**, R14697 (1998).
[34] R.-W. Li, H. Xiong, J.-R. Sun, Q.-A. Li, Z.-H. Wang, J. Zhang, and B.-G. Shen, J. Phys.: Condens. Matter **13**, 141 (2001).
[35] S. Roy, I. Dubenko, D. D. Edorh, and N. Ali, J. Appl. Phys. **96**, 1202 (2004).
[36] T. Zhang, T. F. Zhou, T. Qian, and X. G. Li, Phys. Rev. B **76**, 174415 (2007).
[37] P. Dey and T. K. Nath, Phys. Rev. B **73**, 214425 (2006).
[38] A. Moreo, M. Mayr, A. Feiguin, S. Yunoki, and E. Dagotto, Phys. Rev. Lett. **84**, 5568 (2000).
[39] J. Burgy, M. Mayr, V. Martin-Mayor, A. Moreo, and E. Dagotto, Phys. Rev. Lett. **87**, 277202 (2001).
[40] S. Kaul, J. Magn. Magn. Mater. **53**, 5 (1985).
[41] C. Bagnuls and C. Bervillier, Phys. Rev. B **32**, 7209 (1985).
[42] H. Muller-Krumbhaar, J. Phys. C: Solid State Phys. **9**, 345 (1976).
[43] N. Khan, A. Midya, K. Mydeen, P. Mandal, A. Loidl, and D. Prabhakaran, Phys. Rev. B **82**, 064422 (2010).
[44] N. Khan, P. Mandal, K. Mydeen, and D. Prabhakaran, Phys. Rev. B **85**, 214419 (2012).
[45] S. Saha, S. Bandyopadhyay, and I. Das, J. Alloys Compd. **870**, 159465 (2021).
[46] S. Saha, K. Das, S. Bandyopadhyay, and I. Das, J. Magn. Magn. Mater. **432**, 271 (2017).
[47] See Supplemental Material at http://link.aps.org/supplemental/10.1103/PhysRevB.105.214407 for the brief description of XRD, EDX and critical analysis. This includes Refs. [45,56,58,59].
[48] S. Banik and I. Das, J. Alloys Compd. **742**, 248 (2018).
[49] A. Arrott, Phys. Rev. **108**, 1394 (1957).
[50] B. Banerjee, Phys. Lett. **12**, 16 (1964).
[51] A. Arrott and J. E. Noakes, Phys. Rev. Lett. **19**, 786 (1967).
[52] H. Stanley, *Introduction to Phase Transitions and Critical Phenomena* (Oxford University Press, New York, 1971).
[53] J. S. Kouvel and M. E. Fisher, Phys. Rev. **136**, A1626 (1964).
[54] B. Widom, J. Chem. Phys. **41**, 1633 (1964).
[55] B. Widom, J. Chem. Phys. **43**, 3898 (1965).

[56] M. Getzlaff, *Fundamentals of Magnetism* (Springer, Berlin, 2008).

[57] B. M. McCoy, Phys. Rev. Lett. **23**, 383 (1969).

[58] M. E. Fisher, S.-K. Ma, and B. Nickel, Phys. Rev. Lett. **29**, 917 (1972).

[59] G. Joyce, Phys. Rev. **146**, 349 (1966).

[60] M. Suzuki, Prog. Theor. Phys. **51**, 1992 (1974).

[61] D. A. Sokolov, M. C. Aronson, W. Gannon, and Z. Fisk, Phys. Rev. Lett. **96**, 116404 (2006).

[62] J. Lin, P. Tong, D. Cui, C. Yang, J. Yang, S. Lin, B. Wang, W. Tong, L. Zhang, Y. Zou *et al.*, Sci. Rep. **5**, 7933 (2015).

[63] N. P. Butch and M. B. Maple, Phys. Rev. Lett. **103**, 076404 (2009).

[64] J.-G. Cheng, J.-S. Zhou, J. B. Goodenough, and C.-Q. Jin, Phys. Rev. B **85**, 184430 (2012).

[65] N. Menyuk, P. Raccah, and K. Dwight, Phys. Rev. **166**, 510 (1968).

[66] K. Ghosh, C. J. Lobb, R. L. Greene, S. G. Karabashev, D. A. Shulyatev, A. A. Arsenov, and Y. Mukovskii, Phys. Rev. Lett. **81**, 4740 (1998).

[67] C. V. Mohan, M. Seeger, H. Kronmüller, P. Murugaraj, and J. Maier, J. Magn. Magn. Mater. **183**, 348 (1998).

[68] J. Kumar, S. N. Panja, S. Dengre, and S. Nair, Phys. Rev. B **95**, 054401 (2017).

[69] J. Coey, M. Venkatesan, and H. Xu, *Part 1: Introduction to Magnetic Oxides, Functional Metal Oxides: New Science and Novel Applications*, edited by S. B.Ogale, T. V. Venkatesan, and M. G. Blamire (Wiley-VCH, Weinheim, Germany, 2013).

[70] W. Jiang, X. Zhou, and G. Williams, Europhys. Lett. **84**, 47009 (2008).

[71] S. Banik, N. Banu, and I. Das, J. Alloys Compd. **745**, 753 (2018).

[72] L. Morellon, C. Ritter, C. Magen, P. A. Algarabel, and M. R. Ibarra, Phys. Rev. B **68**, 024417 (2003).

[73] M. Khan, A. Roychowdhury, D. Das, and S. Pal, J. Alloys Compd. **650**, 328 (2015).

[74] A. Bajpai, R. Klingeler, N. Wizent, A. Nigam, S.-W. Cheong, and B. Büchner, J. Phys.: Condens. Matter **22**, 096005 (2010).

[75] R. Mathieu, P. Jönsson, D. N. H. Nam, and P. Nordblad, Phys. Rev. B **63**, 092401 (2001).

[76] I. Fita, I. O. Troyanchuk, T. Zajarniuk, P. Iwanowski, A. Wisniewski, and R. Puzniak, Phys. Rev. B **98**, 214445 (2018).

[77] A. Pal, P. Singh, V. Gangwar, S. Ghosh, P. Prakash, S. Saha, A. Das, M. Kumar, A. Ghosh, and S. Chatterjee, Appl. Phys. Lett. **114**, 252403 (2019).

[78] V. M. Galitski, A. Kaminski, and S. Das Sarma, Phys. Rev. Lett. **92**, 177203 (2004).

[79] Y. Hyun, J. Park, T. Eom, G. Kim, Y. Lee, Y. Lee, V. Prokhorov, and V. Svetchnikov, Appl. Phys. Lett. **93**, 042515 (2008).

[80] T. Eom, Y. Hyun, J. Park, Y. Lee, V. Prokhorov, V. Flis, and V. Svetchnikov, Appl. Phys. Lett. **94**, 152502 (2009).

[81] C. Kittel, *Introduction to Solid State Physics* (Wiley, New York, 2005).

[82] F. Magnus, M. Brooks-Bartlett, R. Moubah, R. Procter, G. Andersson, T. Hase, S. Banks, and B. Hjörvarsson, Nat. Commun. **7**, ncomms11931 (2016).

[83] J. Curiale, R. D. Sánchez, H. E. Troiani, C. A. Ramos, H. Pastoriza, A. G. Leyva, and P. Levy, Phys. Rev. B **75**, 224410 (2007).

[84] M. Wortis, Phys. Rev. B **10**, 4665 (1974).

[85] A. B. Harris, Phys. Rev. B **12**, 203 (1975).

[86] S. Chikazumi and C. D. Graham, *Physics of Ferromagnetism*, 2nd ed. (Oxford University Press, Oxford, 1997), Vol. 94.

[87] N. A. Spaldin, *Magnetic Materials: Fundamentals and Applications* (Cambridge University Press, Cambridge, UK, 2010).

[88] S. Banik, K. Das, and I. Das, RSC Adv. **7**, 16575 (2017).

[89] C. Bean and I. Jacobs, J. Appl. Phys. **27**, 1448 (1956).

[90] C. Bean and U. D. Livingston, J. Appl. Phys. **30**, S120 (1959).

[91] B. Roy and S. Das, J. Appl. Phys. **104**, 103915 (2008).

[92] V. K. Pecharsky and K. A. Gschneidner Jr, Phys. Rev. Lett. **78**, 4494 (1997).

[93] T. Paramanik, K. Das, T. Samanta, and I. Das, J. Appl. Phys. **115**, 083914 (2014).

[94] L. Jia, G. Liu, J. Wang, J. Sun, H. Zhang, and B. Shen, Appl. Phys. Lett. **89**, 122515 (2006).

[95] G. Liu, J. Sun, J. Wang, T. Zhao, and B. Shen, J. Phys.: Condens. Matter **19**, 466215 (2007).

[96] A. M. Tishin and Y. I. Spichkin, *The Magnetocaloric Effect and its Applications* (IOP, New York, 2003).

[97] S. Pakhira, C. Mazumdar, R. Ranganathan, S. Giri, and M. Avdeev, Phys. Rev. B **94**, 104414 (2016).

[98] Y. Duan and J. Li, Mod. Phys. Lett. B **18**, 597 (2004).

[99] T. Sarkar, B. Ghosh, A. K. Raychaudhuri, and T. Chatterji, Phys. Rev. B **77**, 235112 (2008).

[100] C. Dhital, C. de La Cruz, C. Opeil, A. Treat, K. F. Wang, J.-M. Liu, Z. F. Ren, and S. D. Wilson, Phys. Rev. B **84**, 144401 (2011).

[101] K. Sattler, J. Mühlbach, and E. Recknagel, Phys. Rev. Lett. **45**, 821 (1980).

[102] Z. M. Stadnik, P. Griesbach, G. Dehe, P. Gütlich, T. Kohara, and G. Stroink, Phys. Rev. B **35**, 6588 (1987).